Automated segmentation of the atrial region and fossa ovalis towards computer-aided planning of inter-atrial wall interventions

Pedro Morais, MSc [a,b,c,d], João L. Vilaça, PhD [a,b,e], Sandro Queirós, MSc [a,b,d,f], Alberto Marchi, MD [g], Felix Bourier, MD [h], Isabel Deisenhofer, MD [h], Jan D'hooge, PhD [d], João Manuel R. S. Tavares, PhD [c],

[a]Life and Health Sciences Research Institute (ICVS), School of Medicine, University of Minho, 4710-057, Braga, Portugal

[b]ICVS/3B's - PT Government Associate Laboratory, Braga/Guimarães, Portugal

[c] Instituto de Ciência e Inovação em Engenharia Mecânica e Engenharia Industrial, Faculdade de Engenharia, Universidade do Porto, Portugal

[d]Lab on Cardiovascular Imaging & Dynamics, Department of Cardiovascular Sciences, KULeuven - University of Leuven, Leuven, Belgium

[e]2Ai – Polytechnic Institute of Cávado and Ave, Barcelos, Portugal

[f]Algoritmi Center, School of Engineering, University of Minho, Guimarães, Portugal

[g]Cardiomyopathies Unit, Careggi University Hospital Florence, Italy

[h]German Heart Center Munich, Technical University, Munich, Germany

Contacts:

Pedro Morais – pedromorais@med.uminho.pt
João L. Vilaça – jvilaca@ipca.pt
Sandro Queirós – sandroqueiros@med.uminho.pt
Alberto Marchi – alb.marchi@yahoo.com
Felix Bourier – fbourier@googlemail.com
Isabel Deisenhofer – deisenhofer@dhm.mhn.de
Jan D'hooge – jan.dhooge@uzleuven.be
João Manuel R. S. Tavares – tavares@fe.up.pt

Name and Address for Correspondence:

Prof. João Manuel R. S. Tavares
Faculdade de Engenharia da Universidade do Porto (FEUP)
Departamento de Engenharia Mecânica (DEMec)
Rua Dr. Roberto Frias, s/n, 4200-465 PORTO - PORTUGAL
Telf.: +315 22 5081487, Fax: +315 22 5081445
Email: tavares@fe.up.pt Url: www.fe.up.pt/~tavares

Conflict of Interest: The authors declare that they have no conflict of interest.

Automated segmentation of the atrial region and fossa ovalis towards computer-aided planning of inter-atrial wall interventions

Abstract:

Background and objective: Image-fusion strategies have been applied to improve inter-atrial septal (IAS) wall minimally-invasive interventions. Hereto, several landmarks are initially identified on richly-detailed datasets throughout the planning stage and then combined with intra-operative images, enhancing the relevant structures and easing the procedure. Nevertheless, such planning is still performed manually, which is time-consuming and not necessarily reproducible, hampering its regular application. In this article, we present a novel automatic strategy to segment the atrial region (left/right atrium and aortic tract) and the fossa ovalis (FO).

Methods: The method starts by initializing multiple 3D contours based on an atlas-based approach with global transforms only and refining them to the desired anatomy using a competitive segmentation strategy. The obtained contours are then applied to estimate the FO by evaluating both IAS wall thickness and the expected FO spatial location.

Results: The proposed method was evaluated in 41 computed tomography datasets, by comparing the atrial region segmentation and FO estimation results against manually delineated contours. The automatic segmentation method presented a performance similar to the state-of-the-art techniques and a high feasibility, failing only in the segmentation of one aortic tract and of one right atrium. The FO estimation method presented an acceptable result in all the patients with a performance comparable to the inter-observer variability. Moreover, it was faster and fully user-interaction free.

Conclusions: Hence, the proposed method proved to be feasible to automatically segment the anatomical models for the planning of IAS wall interventions, making it exceptionally attractive for use in the clinical practice.

Keywords: Image segmentation; Cardiac Intervention planning; Inter-atrial wall interventions; Competitive segmentation strategy; Atlas-based initialization.

1. Introduction

Anatomically, the atria are complex cardiac chambers with high variability between subjects [1, 2]. Although their body is typically described as simple concave shapes in normal cases [3], atrial enlargement of one chamber is common, negatively affecting the other chamber and changing their anatomies [4]. Moreover, high spatial and shape variations are frequently found in their connected structures (*i.e.* pulmonary veins - PV, vena cava -VC and appendages) and even in specific anatomical regions (e.g. fossa ovalis - FO) [1-3, 5]. Due to all these reasons, minimally invasive atrial interventions are difficult, requiring multiple imaging modalities for planning (mainly computed tomography - CT) and guidance (e.g. ultrasound) [6, 7]. Firstly, during the planning stage, the clinician visually evaluates the richly detailed images, searching for anatomical variations. Next, throughout the intervention, real-time images are used to guide the different instruments inside the human body until the target positions [7].

Traditionally, both planning and interventional data are independently evaluated in a manual manner, being subsequently mentally combined by the expert throughout the intervention [7]. Nevertheless, such approach requires great experience, is very time-consuming, and frequently results in procedural failures and complications [7, 8]. Thus, automated image-fusion strategies were proposed [9, 10]. Usually, these strategies start with a segmentation of the target structures, being subsequently fused with the intra-procedural data [9]. As a result, the high-detail of the pre-operative stage is transferred to the intervention, enhancing and improving intra-procedural images [7, 9].

The success of the aforementioned image-fusion strategies is directly related to the accuracy of the image alignment approach [7]. While some researchers focused on strategies to align the pre- and intra-procedural data using 2D/3D alignment approaches [10], landmark identification [11] and/or image registration [12], other researchers optimized the planning stages suggesting automated algorithm versions [2, 13]. These automated methods showed a performance comparable to the manual analysis [2, 14, 15], requiring none or little user input, removing or minimizing the variability between observers and reducing the time spent during the planning [2]. Specifically for cardiac applications, atlas-based [16, 17], deformable models [14, 18] and machine learning strategies [15] were proposed to segment the different cardiac chambers. Particularly, the methodologies described by Ecabert *et al.* [14] and Zheng

et al. [15] successfully segmented the four cardiac chambers plus the attached great vessels, and the atlas-based methodology from Kirisli *et al.* [16] proved its added-value for cardiac chamber segmentation in large databases of contrast-enhanced [16] and non-contrast-enhanced CT images [19]. However, these solutions still present inaccurate results in the thin mid-walls, showing overlapping regions [16] or merging of different contours [14]. As such, we recently proposed a competitive deformable model strategy to segment the atrial region (*i.e.* atrial bodies and aortic tract - AO) with a correct delineation of the mid atrial walls [18]. Such formulation allowed correct evaluation of the inter-atrial septal (IAS) wall, allowing its application for IAS interventions (e.g. transseptal puncture or atrial septal defect closure) and even improving the planning of multiple minimally invasive atrial interventions (e.g. atrial fibrillation, atrial appendage closure) [5, 20]. However, a semi-automatic version was described in [18], requiring an initialization of each chamber. Moreover, specific landmarks/regions inside the inter-atrial wall, such as FO [5], were not detected.

The fossa ovalis is the thinnest region of the IAS wall, presenting an oval or circular shape and usually located posteriorly, at the junction of the mid and lower third of the right atrium (RA) [6]. It is described as a depression, composed by a thin flap (floor of the FO) and its surrounding margins designated as FO limbus [21]. Since direct physical access to the left atrium (LA) is not possible, the FO is used as an access point between the RA and LA [5, 6]. This technique is termed transseptal puncture, which consists of a needle that is inserted percutaneously until the RA, puncturing the FO and accessing the LA [6]. The correct identification of the FO is crucial to identify the optimal access route between both atria [11], preventing complications, or multiple puncture attempts [5]. Moreover, the FO identification is also relevant in other LA interventions, namely for device selection and optimal route identification for catheter ablation, mitral valve (MV) replacement and left atrial appendage (LAA) occlusion [5, 20, 21]. Some researchers have investigated the added-value of the FO identification in a pre-interventional stage, proving that it eases the real intervention, especially for challenging anatomies [9, 22, 23]. Nonetheless, its identification is still performed manually [9, 22], hampering its application in the clinical practice.

To overcome the aforementioned difficulties, a fully automatic segmentation strategy is proposed in this article to generate the atrial region models and the FO in CT datasets. Both models can improve the current IAS interventional planning, making it faster, more

reproducible and simpler. The method starts by segmenting the relevant cardiac chambers (*i.e.* atrial region) around the IAS wall, allowing an accurate evaluation of wall thickness and shape. The proposed segmentation method is an extension of [18], with a robust initialization through an atlas-based technique. Then, since a correct representation of the IAS wall is used, the FO region is identified by assessing the intermediate mid wall positions of all contour pairs and spatial location information.

Overall, this work introduces three novelties: 1) extension of our previously presented atrial segmentation method with a fully automatic one; 2) a novel methodology to accurately segment the FO; 3) a clinical validation of the proposed method.

This article is structured as follows. In section 2, a technical description of the proposed fully automatic atrial segmentation method is presented. In section 3, the validation experiments and their results are presented. Section 4 discusses the performance of the proposed method against the state-of-the-art and expected inter-/intra-observer variability. Finally, the conclusions of this study are presented in section 5.

2. Methods

The proposed fully automatic method comprises three sequential conceptual blocks (Figure 1): 1) automatic and rough identification of the cardiac chambers through an atlas-based technique with global transformation models; 2) refinement of the target region boundaries using a competitive segmentation methodology that guarantees the integrity of the mid thin walls; and 3) identification of the FO region through the combination of the

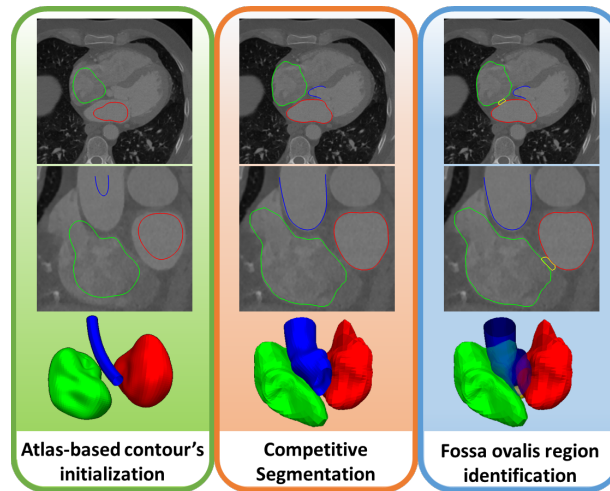| Atlas-based contour's initialization | Competitive Segmentation | Fossa ovalis region identification |

Figure 1 - Overview of the proposed fully automatic method for atrial region segmentation (red: LA, green: RA, blue: AO) and fossa ovalis identification (yellow).

patient-specific wall thickness information (extracted from the anatomical models obtained in (2)) and a set of known anatomical references that provides the spatial location.

2.1. Atlas based contour's initialization

Due to the high feasibility previously demonstrated by atlas-based techniques [16], a similar methodology was selected to initialize our method. The traditional formulation finds the optimal transformation that aligns the target image with a labelled dataset (designated as atlas), subsequently applying it to the labels and transferring the relevant anatomies to the target image. Different transformation models have been used, for example, global transforms (rigid or affine) are used to roughly align the different cardiac cavities and local transforms (deformable registration) are then applied to adapt the results toward the anatomy [16, 17]. Since anatomical variations are expected, multiple atlases are usually used and all the results are combined through a label fusion process. However, the current strategies still present disadvantages: they are very time-consuming, the resulting shape variability is dependent of the atlases used, the target and atlas image should present a similar field of view (FOV) and should be in the same cardiac phase [2, 16, 17].

Taken into consideration all the aforementioned drawbacks, we modified the traditional atlas-based approach [16] through:

1 - A pre-processing strategy that defines a FOV around the heart region (Figure 2a). The method defines a bounding box using the lung positions, which are binarized through the Hounsfield units (HU). The inferior limit of the bounding box is defined by the inferior tip of the lungs and its central position is defined by the centroid of both binarized lungs. Of note, the lungs were selected, since they are always visible on cardiac CT images and due to its particular HU value.

2 – Instead of global and local registrations, the current strategy only applies affine transforms, allowing a fast initialization of the cardiac anatomy. Moreover, a two-stage sequential process is used: i) a full image and ii) a regional (left or right heart) alignment. The full image approach aligns the entire image (target image and atlas), initializing all chambers simultaneously (Figure 2b). The resulting contours are then applied to mask the left (Figure 2c) and right heart (Figure 2d) in the target image. In order to prevent overlaps between the left and right alignment stages and to compensate sub-optimal global alignments,
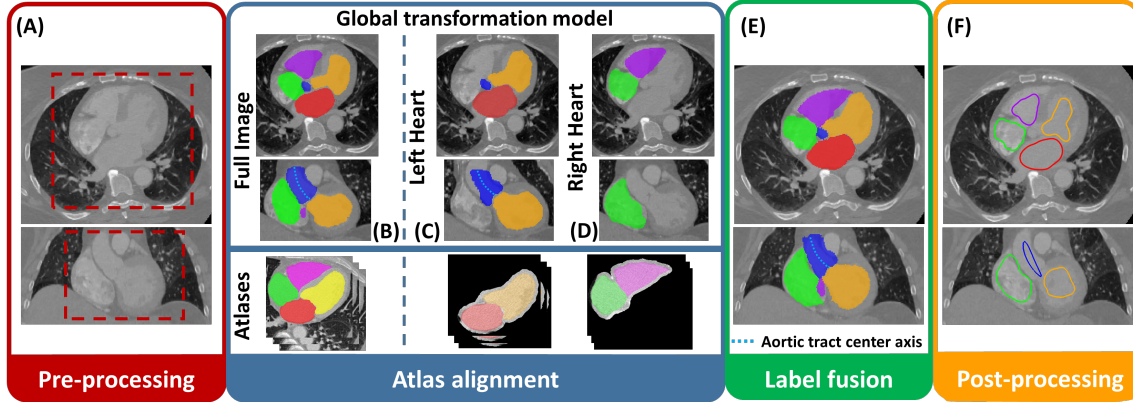
6

Figure 2 - Atrial region initialization through an atlas-based strategy. (A) Cropping of the heart region; Global alignment using the (B) full cropped image and the (C) left and (D) right heart. (E) Label fusion using a majority voting and final post-processing of each label (F).

each masked region is dilated (in our experiments, by 10 mm). Finally, both regions are independently aligned with masked left and right atlases, respectively.

3 – The AO center axis (defined as 5 points) is also transferred to the target image (dashed line in Figure 2) using the optimal transformation. The axis is later referred to in section 2.2.1.

4 – The final label fusion is performed for all organs at once using a majority voting [24] (Figure 2e). Next, a post-processing based on Otsu threshold is applied [25] (Figure 2f), improving the robustness of the method for sub-optimal results. In detail, the preliminary result of each chamber is used to mask the image, and each masked region is then divided into two groups based on its image intensities. The group with the largest number of voxels is selected as the final result. Specifically for the AO, we fit a spline to all possible points obtained previously.

5 – Two atlas database are used: i) a public database [16] with 8 atlas at end-diastole (ED), and ii) an *in-house* database with 4 atlas at end-systole (ES). The phase of the target image should be selected or extracted from the acquisition parameters.

2.2. Competitive Segmentation

The proposed segmentation method relies on our previously developed atrial region segmentation strategy [18]. A set of independent functions are used to control the evolution of each 3D contour (*i.e.* LA, RA, AO, left ventricle - LV, right ventricle - RV), and a set of image descriptors are used to identify the optimal boundaries. The segmentation problem is
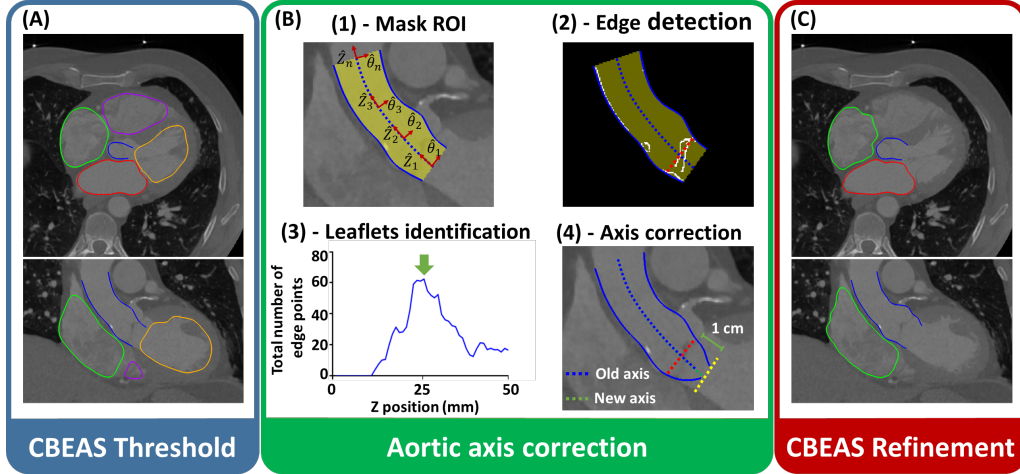
Figure 3 – Pipeline of the segmentation strategy. (A) Fast contour growing using threshold-based competitive B-spline Explicit Active Surface (CBEAS); (B) Aortic axis correction; and C) Contours refinement using local CBEAS. $\hat{\theta}$ and $\hat{z}$ represents the coordinates of the cylindrical space.

an iterative process guided by intensity-based (signed local Yezzi – SLY, [26]) and edge-based energies (unsigned distance function to the nearest edge). The edge map is generated using a Canny edge filter. In order to prevent overlapping regions, a competitive approach is applied between all the contours pairs. In detail, when the distance between two contours is lower than a pre-defined value (R_T), a force with opposite direction to the propagation direction is applied to each contour, locally preventing fast steps or even changing the contour evolution direction. The magnitude of the competitive force is computed based on the distance between contours, assuming a small value when the distance between contours is near R_T (allowing refinement to mid walls) and applying a high penalization (preventing overlapping) when the distance is almost zero.

In order to make the method computationally attractive, the B-spline Explicit Active Surfaces (BEAS) framework is used [27]. As such, each contour uses an analytic representation described as a linear combination of B-splines. Furthermore, explicit functions (cylindrical model for the AO and spherical representation for the remaining contours), and independent smoothing terms are applied to each contour, reducing the dimensionality of the segmentation problem and allowing independent control of the smoothing degree of each contour, respectively.

The segmentation pipeline relies on [18], namely: 1) fast growing of the initialized contours using a competitive BEAS (CBEAS) threshold with global descriptors (Figure 3a); 2) AO axis correction (Figure 3b); 3) contour refinement using the CBEAS segmentation

8

with local descriptors (Figure 3c). Note that that the LV and RV contours are only evolved throughout the first stage to define the valve planes. Moreover, contrary to [18], an axis correction stage (section 2.2.1) is now included to compensate for sub-optimal AO axis results throughout the section 2.1.

As the output of this step, a set of meshes S_i with $i \in \{LA, RA, Ao\}$ are obtained. Each mesh is represented by multiple vertices $x = [x, y, z]$ and a connectivity matrix c.

2.2.1. Aortic Axis Correction

The atlas-based technique allows a coarse identification of the AO axis, presenting a sub-optimal performance in the left ventricular outflow tract (LVOT) region, due to the lack of walls. Inspired by [13], we propose an AO axis correction technique. The method starts by estimating the leaflets positions through a Canny edge filter (Figure 3B-2) applied on a region-of-interest (ROI). The ROI is defined based on the AO contour computed at the BEAS-threshold stage (Figure 3B-2). Then, the obtained edge map is represented in the cylindrical space. For each $\hat{z}$ level, the number of $\hat{\theta}$ coordinates with an edge point is counted, and the level with the maximum number of edges is used to define the leaflets regions (Figure 3B-3). Finally, we generate a novel axis assuming a fixed spacing (in our results this spacing was defined equal to 10 mm) between the leaflets and the LVOT plane (Figure 3B-4), and reinitialize the AO contour.

2.3.   Fossa ovalis identification

The FO is identified by the evaluation of two different parameters (Figure 4): i) IAS wall thickness (section 2.3.1), computed using the boundary of the atrial contours; and ii) spatial location of the expected FO region (section 2.3.2), aligning the obtained anatomical atrial surfaces with manual delineated references that contain the FO region. While the first parameter provides accurate anatomical information, the second one computes a smooth voting map that represents the FO spatial variation. Thus, by combining both parameters, local minima caused by incorrect segmented regions or incorrect spatial locations are penalized, enhancing the real FO region.

In order to simplify the searching of the FO region, the proposed method is applied to the LA surface only. In this sense, the FO at the left heart is initially located, and then interpolated towards a 3D volume using the spatial relation between chambers. It might be
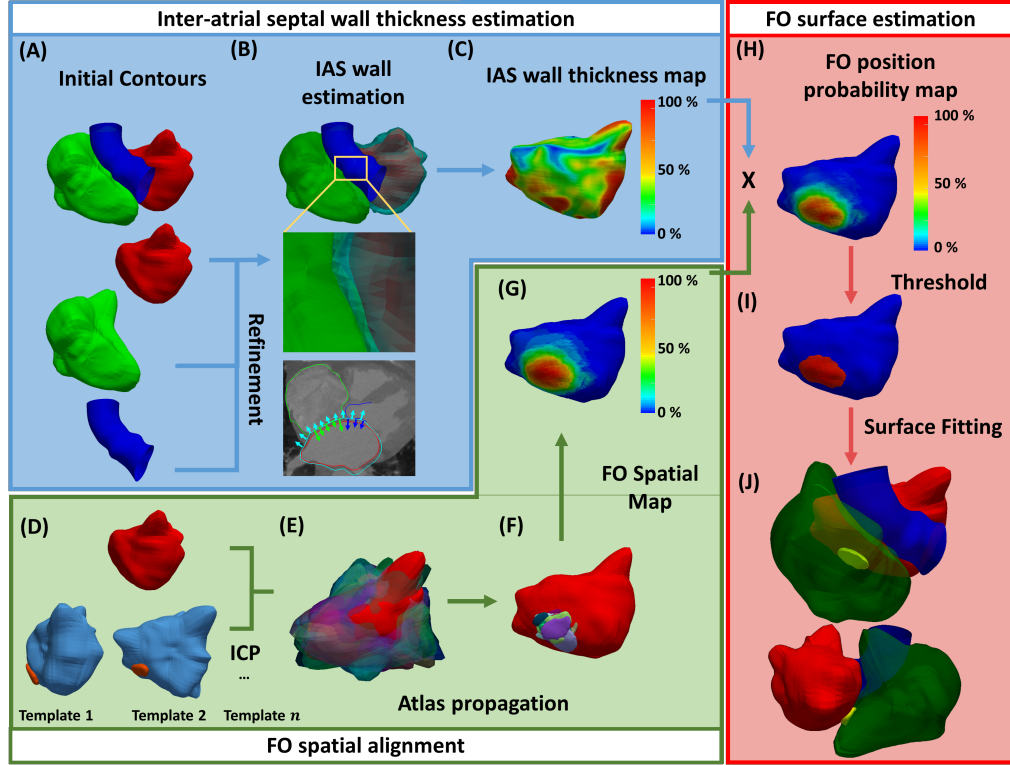
9

Figure 4 – Strategy to automatically identify the fossa ovalis (FO). The method starts by (B) estimating a wall surface (cyan contour) based on the original contours (A) and (C) computing the distance between the IAS and the LA (red contour) contours to define the IAS_{Thick} map. (D) The LA contour is also aligned with a set of templates with known FO region through an iterative-closest-point (ICP) strategy. (E-F) All the template results are combined into one generating the $FO_{Spatial}$ map (G). (H) Both maps are finally merged and a threshold is used to binarize the optimal region (I). A surface fitting (yellow surface) is applied to reconstruct the FO (J).

noted that the LA contour is used due to its superior image quality and higher segmentation accuracy [18].

2.3.1. Inter-atrial septal wall thickness estimation

In order to estimate the IAS wall thickness, an extra segmentation process is applied focused on the mid walls. Although this information could be extracted from atrial contours, its result is dependent on the segmented anatomical regions in all chambers. Since the FO region is located near the intersection between the inferior vena cava (IVC) and the RA body (when evaluated from the right heart), its accurate detection is hampered due to a sub-optimal RA segmentation result in the IVC. In this sense, a new contour focused on the particularities of the IAS wall shape is initially and evolved (Figure 4b). This contour is defined based on the LA position and its evolution is controlled by the previously obtained atrial models (Figure 4a). Thus, the wall details found between the atrial contours are directly integrated

on the final IAS surface, and also applied to accurately estimate the wall thickness in regions with sub-optimal segmentation result.

Starting from the LA contour, an extra BEAS surface representing the wall thickness is initialized (Figure 4b). Both surfaces are combined using a coupled strategy (Figure 4c), meaning that the wall surface is represented based on the LA contour position (ψ^{Pos}) plus the wall thickness (ψ^{Thick}). The reader is kindly directed to supplementary material I and for [28] for further details on coupled methodologies in the BEAS framework.

The original LA contour is not updated throughout this stage, working only as an anchor for the segmentation of the mid-walls and keeping the ψ^{Pos} unaltered. As such, a novel optimization process targeting the identification of the optimal thickness map ψ^{Thick} is started. Specifically, the evolution of the IAS contour is guided by a SLY energy (targeting black to white transitions) with no edge terms. Negative thicknesses are not allowed, preventing overlaps between both LA and IAS contours [26].

In order to ease the wall boundaries identification, a competitive strategy is also applied between the IAS contour and the RA and AO contours. Again, the RA and AO are not optimized during this stage, working as a barrier. Since no empty spaces are physically expected between the IAS wall and the AO|RA, the R_T was set to 0 mm, penalizing overlapping regions only.

The wall thickness map $IAS_{Thick}(\boldsymbol{x})$ is finally defined at the vertices $\boldsymbol{x}$ of the LA contour and computed as the distance between S_{LA} and the IAS wall contours (Figure 4c). Finally, relative distances are computed by normalizing the value in each vertex by the maximum value in the map.

2.3.2. Fossa ovalis spatial alignment

The FO spatial location is estimated based on a surface alignment technique applied between the automatic and a set of references/templates with the desired anatomy. The references correspond to datasets manually evaluated by one expert, which includes both LA and FO surfaces (Figure 4d). In detail, the target LA chamber is aligned with a set of LA references using an iterative closest point (ICP) strategy (Figure 4e). We start by rigidly aligning both surfaces and then compensating the scaling differences using a similarity transform. The final transform for each case is independently applied to the FO label,

propagating it to the target LA (Figure 4f). Then, the distance between each point of the transformed FO surface and the vertices x of the automatic LA is computed, and the nearest LA vertices considered as valid FO points.

Finally, a voting map $FO_{Spatial}(x)$ is constructed, by counting the different number of FO templates in each vertices x and normalizing it with the maximum value (Figure 4g).

2.3.3. Fossa ovalis surface estimation

FO probability map estimation and binarization: The final probability map is obtained by combining both IAS_{Thick} and $FO_{Spatial}$ maps in each vertices x through (Figure 4h):

$$FO_{Position}(x) = (1 - IAS_{Thick}(x)) \times FO_{Spatial}(x). \tag{1}$$

Both IAS_{Thick} and $FO_{Spatial}$ are normalized between [0-1], with 1 representing the maximal thickness position and the optimal anatomical location of FO, respectively. By inverting the IAS_{Thick} map and multiplying it with the $FO_{Spatial}$, the FO region is enhanced.

Finally, the optimal position of the FO is extracted from the $FO_{Position}$ map, by applying a relative threshold value (Figure 4i). All the positions x with a value higher than this threshold are considered as valid FO points.

FO surface fitting: Starting from the valid FO points, a 3D FO surface is reconstructed based on the spatial relations between the chambers. As such, we compute the distance between each FO point and the remaining surfaces (*i.e.* RA and AO). In detail, for each selected point, the nearest position is selected as a valid FO boundary, generating a point cloud representing the FO anatomy. Finally, a structured surface is estimated by deforming an ideal spherical mesh with the point-cloud through [29] (Figure 4j).

3. Experiments

The new fully automatic framework (henceforward referred as FA) was evaluated based on: 1) the differences found between the FA atrial region segmentation strategy relatively to the previous validated semi-automatic technique (termed SA) and manual contours; and 2) the analysis of the FO estimated by the proposed strategy and the corresponding one manually delineated.

3.1.   Data description

Forty-one datasets retrospectively obtained in clinical practice from patients with suspicion of pathology in the atria were used. In detail, patients with normal anatomy, pacemaker, prosthetic valves, atrial body enlargement and candidates to pulmonary vein ablation were included. ECG-gated cardiac multi-slice CT images were acquired with a multi-detector SOMATOM Force (Siemens, Germany) CT scanner, with the number of rows varying between 64-128 slices. An image resolution of 0.69x0.69 mm^2, slice thickness of 0.8 mm, and a matrix size of 512x512 was used. The X-ray tube current varied between 1844-2597 mA and the peak voltage varied between 70-110 kV. A contrast injection (Imeron 350, Bracco-Byk Gulden, Konstanz, Germany) of 40-100 ml was applied and a unique phase was acquired (both end-diastolic and end-systolic phases were included). Each dataset was reconstructed using the convolution kernel Bv36d. All the described acquisition parameters were defined based on the normal clinical practice at the German Heart Centre Hospital. An overview of the clinical dataset cases can be found in Supplementary Material II.

3.2.   Fully automatic atrial region segmentation

Ground truth generation: Both LA and RA contours were manually delineated by one expert using the semi-automatic CARTO3 segmentation tool (Biosense Webster, Diamond Bar, CA, USA), followed by manual corrections (as described in detail in [9]). The AO was manually delineated using an *in-house* software through the following steps: 1) AO centerline definition, by providing multiple clicks along the AO tract; 2) delineation of multiple planes (25-30 planes) perpendicular to the centerline and, 3) surface reconstruction. Moreover, similarly to our initial work, multiple bounding boxes were manually generated using a 3D visualization software (Paraview Kitware Inc., USA [30]), limiting the influence of the connecting structures of the atrial body, i.e., PV, VC and left/right atrial appendages (LAA/RAA), in the final result of the proposed method. Note that each bounding box was generated around the ostia of each structure. Moreover, two planes representing the mitral and tricuspid valve (TV) were built and used to evaluate the accuracy of the proposed atrial body segmentation method. In detail, each plane was independently defined using the following strategy: 1) manual delineation of the valve's ring in several rotated planes (centered on the valve center position); and 2) plane fitting to these points.

Implementation details: The regular bounding box used to define the FOV in CT images (section 2.1) had a size of 20 x 20 cm along the axial direction, and its height was computed as the distance between the lung's centroid and the lung's tip. Regarding the segmentation parameters (section 2.2), all were kept from the original work [18]. The reader is kindly directed to [18] for further details on them.

Statistical analysis: The FA contours were compared against the corresponding manual and SA results (available in [18]) in terms of absolute point-to-surface (P2S) distance, Dice coefficient (DC) and 95th percentile of the Hausdorff distance. Moreover, the influence of the generated bounding boxes and valve planes to separate the atrial body from its connected structures was also evaluated. Regarding the FA results, independent databases were used to initialize the method through the abovementioned atlas-based strategy (section 2.1). Note that, in contrast to our previous study [18], where the same AO center axis was used for the manual and the SA method, the new method automatically estimates the AO axis. Thus, the AO result was evaluated using the entire surface and the common region only (*i.e.* clipping both automatic and manual surfaces with the surface's limits). A paired *t*-test (p<0.05) between the SA and FA errors when compared with manual contours was used to check for statistically significant differences in the results. Moreover, the error obtained for each stage of the FA error was also evaluated and compared with a paired t-test (p<0.05). Finally, the computational time of the FA approach was registered. All results were computed using MATLAB code on an Intel (R) i7 CPU at 2.8 GHz and 16 GB of RAM. A C++ implementation of the competitive strategy and of the registration algorithm [31] was used.

Results: Table 1 shows the differences between the results obtained by the FA and the manual approaches. Of note, the FA was not feasible in two cases, namely: in one case the AO axis was wrongly initialized (entering inside the superior vena cava), and, in another one, the TV valve was wrongly estimated. Moreover, the SA results were also presented against the ones obtained by the FA version, showing a similar performance for the LA and RA segmentations. Again, the maximal accuracy was obtained for the LA chamber with an error of 1.05±0.19 mm (FA version). A notable improvement was observed for the AO (SA vs FA), achieving not-statistically significant differences only for the clipped version.

Figure 5 presents the FA segmentation error in each stage of the proposed method, showing a significant reduction of the error between all steps. Finally, representative FA

Table 1 – Point-to-surface (P2S) error, Dice coefficient and 95th percentile of Hausdorff distance obtained between the proposed method (semi-automatic – SA and fully automatic – FA) against manual contours for atrial region segmentation.

	Segmentation	P2S (mm)		Dice		95th perc. Hausdorff (mm)	
		SA	FA	SA	FA	SA	FA
LA	Entire	1.54 ± 0.32	1.52 ± 0.33	0.91 ± 0.01	0.91 ± 0.01	6.52 ± 2.41	6.64 ± 1.75
LA	Cropped	1.07 ± 0.17	1.05 ± 0.19	0.95 ± 0.01	0.95 ± 0.01	3.36 ± 0.98	3.38 ± 0.80
RA	Entire	2.13 ± 0.51	2.17 ± 0.54	0.87 ± 0.03	0.86 ± 0.04	8.13 ± 2.18	8.10 ± 1.98
RA	Cropped	1.68 ± 0.47	1.69 ± 0.35	0.91 ± 0.02	0.92 ± 0.02	6.03 ± 2.04	6.11 ± 1.34
AO	Entire	0.65 ± 0.12*	0.83 ± 0.44*	0.94 ± 0.02*	0.91 ± 0.05*	1.61 ± 0.33*	2.28 ± 1.71*
AO	Clipped	-	0.71 ± 0.38	-	0.94 ± 0.04	-	1.87 ± 1.46

* paired t-test between the FA and SA result (p<0.05). LA – Left atrium, RA – Right atrium, AO – Aortic tract;
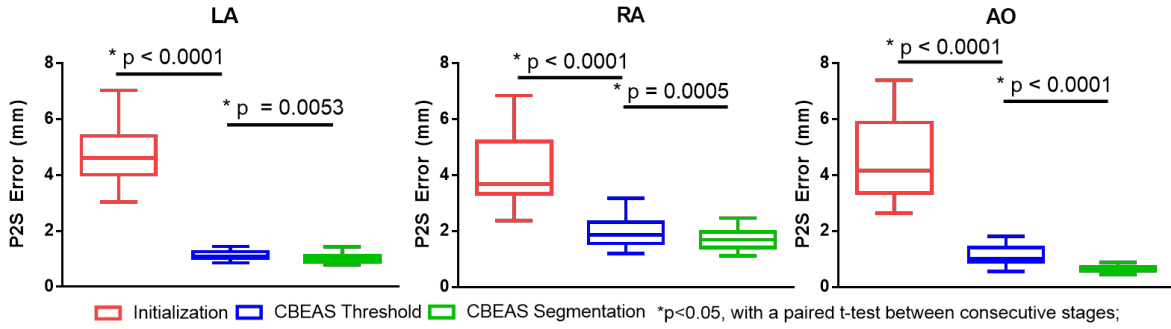

Figure 5 - Point-to-surface (P2S) error obtained throughout the different stages of the fully automatic segmentation method, namely: i) Initialization of the contours (red); ii) fast contour growing (blue) and iii) contour refinement (green).

segmentation results are shown in Figure 6. For clarity sake, we also presented the IAS wall contour (cyan contour) which is applied to estimate the FO region. Regarding the computational time, the contours initialization through an atlas-based technique took 61.4±5.1 seconds, while the competitive segmentation required 42.1±6.0 seconds. The manual analysis made by the expert took approximately 10 minutes per patient.

3.3. Fully automatic identification of the fossa ovalis region

Ground truth generation: Two experts (Obs. 1 and Obs. 2) identified the FO region in all the 41 datasets. Moreover, one expert repeated the analysis for 10 cases two weeks later. In detail, multiple 2D slices of the FO were delineated and then interpolated into a 3D surface. Manual corrections were finally performed to improve the result. The manual delineation strategy was performed using the MITK (Medical Imaging Interaction Toolkit, [32]).

Implementation details: Here, the IAS contour (section 2.3.1) was defined using a spherical representation with a total of 40 × 40 points and the regional intensity-based energies were defined using image profiles with 3 mm inward and outward of the contour.
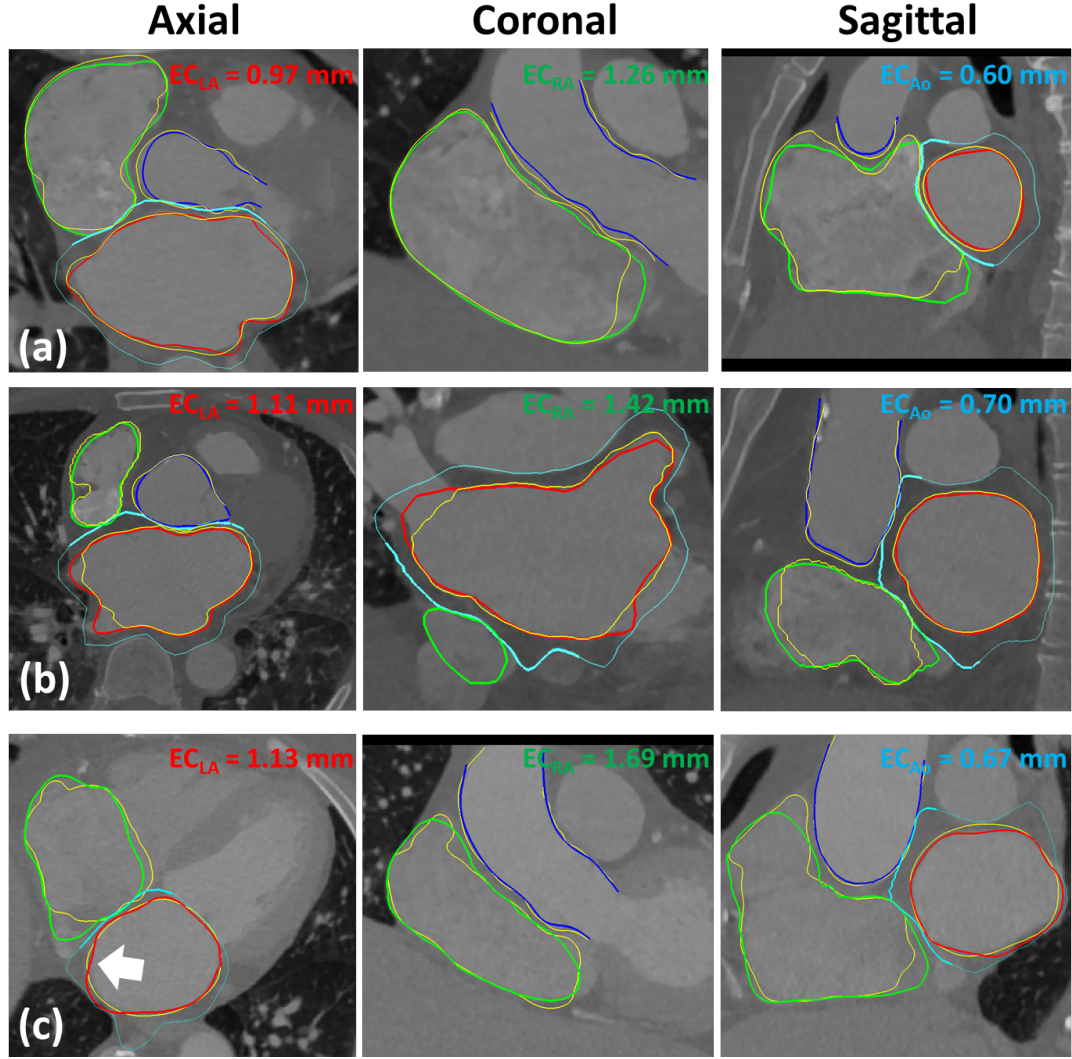
Figure 6 – Automatic segmentation results for the cases corresponding to the (a) 25th, (b) 50th and (c) 75th percentile according to the point-to-surface (P2S) distance (red: LA, green: RA, blue: AO, cyan: inter-atrial wall, yellow: ground truth). EC represents the P2S error obtained with a cropped contour.

The $FO_{Spatial}$ map was estimated using all manually evaluated CTs as temples using a leave-one-out strategy (*i.e.* the target case was removed from the database). The influence of the number of templates used is addressed in Supplementary Material III. Regarding the relative threshold (section 2.3.3), the 90th quartile of the probabilistic map was used. It should be noted that the threshold was defined without the positions with probability equal to 0. For further details about parameter tuning, the reader is kindly directed to the supplementary material III.

Statistical analysis: The FA results were compared with the corresponding manual contours in terms of P2S, Dice and centroid position error, *i.e.* computed as the distance

between the centroid of both surfaces (CPE). The intra- and inter-observer variability was computed using the difference between the manual analysis, and compared with the FA results using an unpaired and paired t-test (p<0.05), respectively. Finally, the computational time was registered and compared with the manual practice.

Results: The FA method was able to estimate successfully the FO in all the 41 cases. Overlaps between FA and manual surfaces were always obtained and the optimal FO position (maximum value of $FO_{Position}$) was always found inside the manual contours. Figure 7 shows the intra- and inter-observer variability and also the evaluation results of the FA method against the manual analysis in terms of P2S, Dice and CPE. A similar performance was found between the FA method and inter-observer variability for the P2S (intra-observer: 1.39 ± 0.35 mm, inter-observer: 1.74 ± 0.68 mm, FA-Obs1: 1.77 ± 0.66 mm and FA-Obs2: 1.88 ± 0.58 mm) and Dice (intra-observer: $70.66 \pm 4.74\%$, inter-observer: $65.40 \pm 9.08\%$, FA-Obs1: $60.92 \pm 11.92\%$ and FA-Obs2: $61.33 \pm 9.06\%$). Statistically significant differences
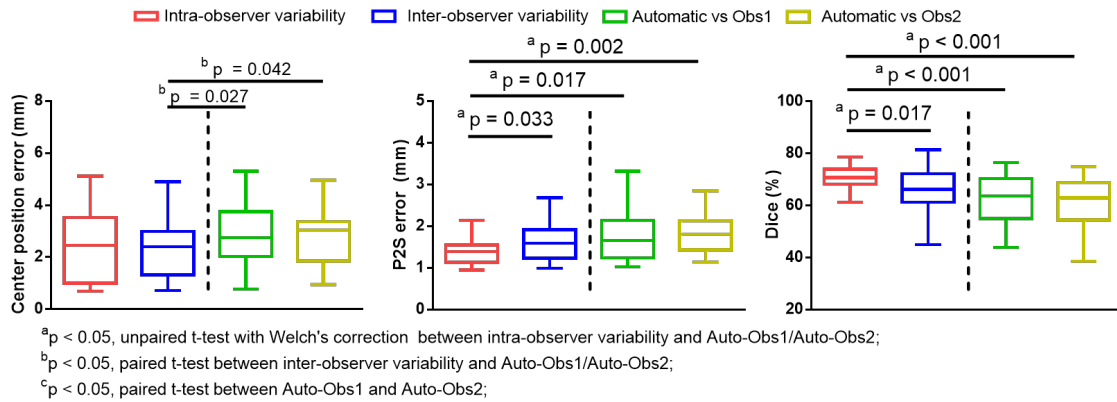

Figure 7 – Evaluation of the accuracy of proposed fossa ovalis estimation method. The centroid position error, point-to-surface error (P2S) and Dice were applied to evaluate the fully automatic (FA) method against two manual observers (Obs1, Obs2). The intra- and inter-observer variability is also presented.
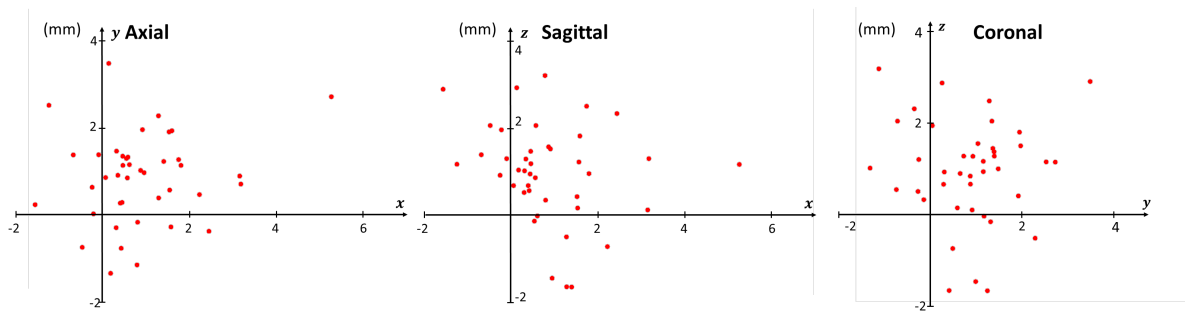

Figure 8 – Distribution of the spatial centroid position errors (axial, coronal and sagittal directions) between the mean manual results and the automatic ones.

were found between the FA evaluation and the inter-observer variability for the CPE error (intra-observer: 2.50 ± 1.37 mm, inter-observer: 2.43 ± 1.20 mm, FA-Obs1: 2.90 ± 1.28 mm and FA-Obs2: 2.90 ± 1.17 mm). Figure 8 allows the assessment of these differences by showing the spatial distribution of the CPE. In detail, the error between the manual (mean of both observers) and the automatic centroid in each spatial direction (*i.e.* axial, sagittal and coronal) was computed. A clear tendency to generate the FO contour superiorly was found with the manual method when compared with the FA one. Figure 9 shows representative FO results. Finally, the FA required 15.0 ± 1.6, 21.3 ± 1.9 seconds for the spatial location map and 0.7 seconds for the algorithm's steps 2.3.1, 2.3.2, and 2.3.3, respectively. The manual delineation took approximately 4 minutes per patient.
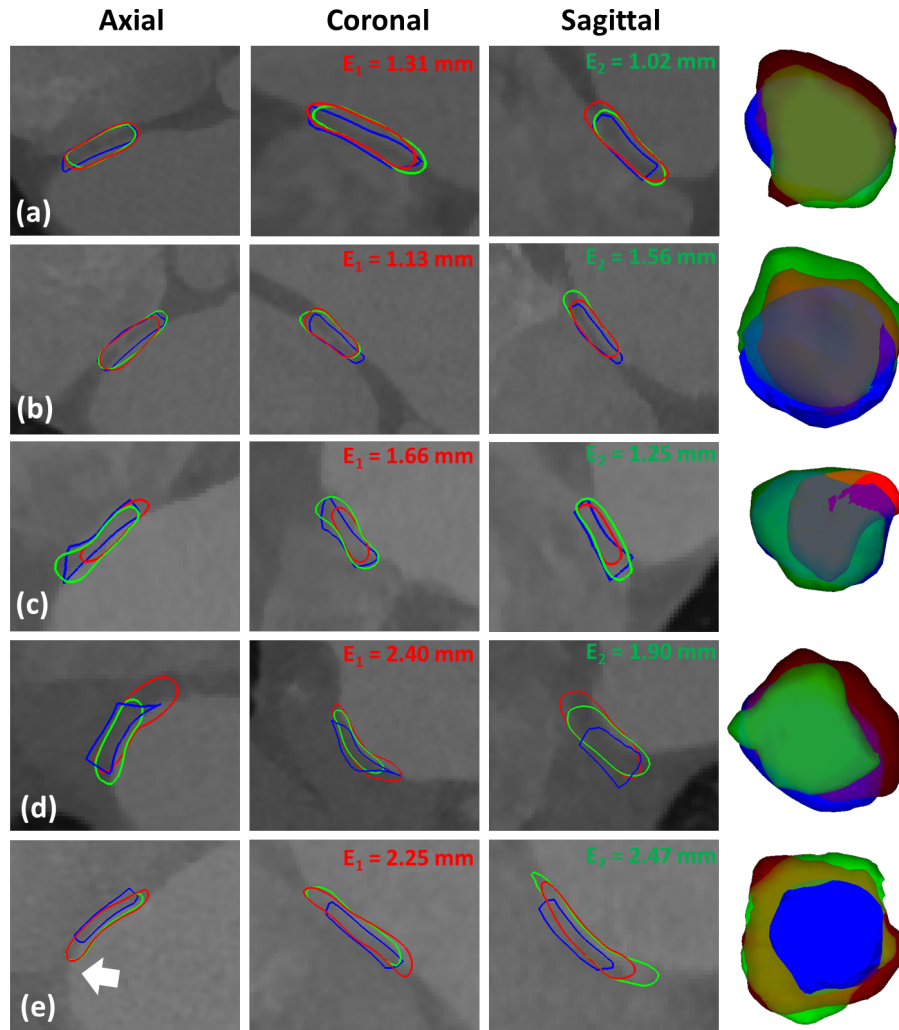

Figure 9 – Estimation of the fossa ovalis region (in blue) by the automatic method (FA). The presented cases correspond to the (a) 10th, (b) 30th, (c) 50th, (d) 70th and (e) 90th percentile according to the point-to-distance (P2S) error. The difference between FA and each manual observer (red: Obs1 and green: Obs2) is also presented (E_1 – FA/Obs1, E_2 – FA/Obs2).

4.   Discussion

In the article, we present a novel fully automatic strategy to segment both atrial region models and the fossa ovalis. The proposed method is divided into three sequential stages with a robust initialization through the use of an atlas, atrial chambers segmentation and mid-walls using a competitive approach and anatomical landmark identification by combining wall thickness information and spatial landmark location. Globally, the proposed framework showed a high feasibility and accuracy, corroborating its added-value for IAS intervention planning. Although in two independent cases the segmentation was considerable not feasible, possibly requiring a small user input correction, acceptable results were achieved for all the FO surfaces. Note that, no user-input was allowed and all results were obtained without any user interaction. Indeed, since an accurate delineation of the atrial and aortic walls was still achieved in these two cases, correct identification of the FO was possible.

The importance of a correct IAS intervention planning through identification of relevant landmarks was previously described [9, 22, 23, 33, 34]. In addition to be crucial in abnormal anatomical situations, correct planning also improves the physician's confidence, reduces the number of procedural failures, eases the entire intervention, and improves the intervention result [5, 9, 33]. Nevertheless, the planning stage is usually performed manually [9, 22], which is extremely time-consuming (taking more than 14 minutes per patient) and presents high intra-/inter-observer variability, hampering its application during clinical routine. In this sense, the proposed FA strategy appears as a potential and promising solution, showing high robustness, accuracy and low computational burden (full planning requires 2-3 minutes). Regarding its computational cost and taking into consideration the expected high variability of the FOV used in clinical CT acquisitions (*i.e.* cardiac region only, full thorax, full body, among others), different strategies were implemented to reduce the influence of the number of samples used (i.e. image size) in the computational burden of the proposed method, namely: 1) pre-processing of the entire image to detect a target FOV throughout the atlas alignment stage; 2) competitive segmentation using regional-based energies defined based on the contour's position; and 3) FO identification totally based on 3D surfaces only. To the author's best knowledge, no previous work focusing on the automatic planning of IAS interventions was presented, being a clear novelty of this work. Currently, few software tools are available to evaluate all cardiac chambers and even great vessels [14, 15]. However,

evaluation of the atrial/aortic walls is not possible [14, 17]. Finally, and in a different way, some researchers are now exploring the potentialities of novel augmented reality setups, fusing multiple imaging modalities, to ease the visual identification of the FO [21].

Starting to evaluate the proposed segmentation method, the combination of both global atlas alignment with a refinement through a competitive strategy showed its high accuracy and feasibility (Table 1), with a performance comparable to other automatic methods [15] [14, 16]. Additionally to the described clinical database, the method's accuracy was also corroborated in one recent benchmark (STACOM 2013 [2], supplementary material IV), allowing a direct comparison between the errors obtained by the FA method and the variability between manual observers, which was not possible by the clinical database used. Similarly to our previous study [18], the RA showed the highest errors (approximately 1.7 mm for the FA and SA), which is explained by the noisy regions found, the difficulty in distinguishing between VC and atrial body, and even low contrast or missing walls at the TV valve plane. No differences were achieved between the SA and FA methods for the LA and RA results. A similar performance between FA and SA methods was observed for the entire and cropped contours situation (Table 1 and Figure 6). In contrast, significant differences were found between the SA and FA for the entire AO contour, due to the initialization used in the new method (Table 1). While both SA and manual contouring were performed using the same centerline, the FA estimates the AO axis totally based on the image content (coronal view of Figure 6a). As such and as previously observed in other studies [13, 35], small differences between central axis will result in high P2S errors. When evaluating the common AO region, *i.e.* clipped version, no statistically significant differences were found, proving that the lower performance found for the FA is related to the initialization strategy applied. Regarding the computational time, and similar to the previous observed in [18], the segmentation through a competitive based BEAS approach corroborated its low computational time (less than 1 minute to segment the LA, RA and AO) and attractiveness for normal clinical practice.

Similarly to the multi-atlas segmentation strategies [16, 17], the high feasibility of the proposed method is related with the atlas-based technique applied and its atlas database. Only a rough estimation of each chamber (by identifying its central region) is required by our methodology, being posteriorly refined to the real anatomy based on the spatial location of

the multiple contours (Figure 5). As such, the result of the proposed method is theoretically not so sensitive to the atrial anatomical shape variability available in the atlas database, as observed for the totally-based multi-atlas case. In fact, our methodology appears to be more versatile for atrial region segmentation when compared with pure atlas-based techniques, particularly in abnormal cases. Note that the clinical database was constructed by retrospectively and sequentially selecting datasets from the hospital database. Therefore, a high shape variability and even different image properties are found between the different subjects, including normal and multiple pathological cases (supplementary material II). Regarding the computational time, the proposed method is much faster (approximately 2 minutes in a common personal computer laptop) than traditional atlas approaches, making it more attractive for clinical practice. However, the authors would like to mention that the multi-atlas strategies are generic formulations with a large application in different scenarios (not only the heart) [24] and without any model description limitation [16, 17]. Moreover, although we considered our method to be fast, optimized tools that segment all chambers in a few seconds are available [14, 15].

In a second stage, we presented a novel strategy to extract relevant landmarks from the aforementioned atrial models. Since the automatic FO detection stage is totally dependent of the initial contours, the current FO strategy is not feasible without an accurate segmentation process. Contrary to previous studies where the FO is visually detected [34, 36], either by manually marking on one specific image position [37], or by identifying the thinnest position of the atrial wall in two/three orthogonal planes [22], we automatically extract an entire 3D surface showing the extent of the FO region. This realistic surface can be used to facilitate and improve the detection of the optimal access routes for transseptal puncture by identifying the optimal position that guarantees maximum catheter dexterity at the left side [9, 23, 36, 38], as a relevant landmark region for IAS defect closure [39] and for optimal device selection for other LA procedures [6, 20, 21]. In order to identify the FO, we combined both patient-specific information, measured as the IAS wall thickness and spatial maps representing the expected FO position. The IAS wall thickness is defined based on the initial atrial contours, being used as fixed references. Although the FO contour is defined along the LA surface, only the points at the interaction positions (and its neighbors, dark cyan line in Figure 6) between the different contours are relevant for the identification of the FO. In order

to obtain a high detail on IAS wall, low smoothing terms were applied, making it correctly defined for the IAS region but a little jaggy for the remaining regions.

Regarding the FO spatial map strategy, it aligns the unknown case with a set of different anatomies, transferring the labeled FO for the novel patient. Although such strategy makes the results dependent on the anatomies available in the template database, it only generates a global map describing the anatomical regions where the FO can be found. Indeed, the influence of the number of cases used on the template database was also evaluated, obtaining a similar performance when using half or the entire database, corroborating therefore the method's robustness (supplementary material III). It might be noted that the computational cost of this step is directly related to the number of templates used. Nevertheless, since we only need to estimate a global map of the FO location, a high number of templates is not required, thus keeping the method computationally attractive. Then, and in order to adapt the result to the particularities of each patient, the global map is refined using the patient-specific anatomy extracted from the wall thickness map. In fact, accurate detection of the FO region using only the spatial or thickness map is not feasible (supplementary material III). Therefore, the combination of both IAS wall thickness and the spatial maps is required to compensate for possible segmentation errors, generating a probabilistic map that represents the optimal FO positions. Moreover, the application of one spatial map is also crucial to make the current strategy less sensitive to the image acquisition parameters (e.g. differences in terms of contrast). As a final remark, although the obtained probabilistic map could be directly used as a relevant reference for interventional planning, we decided to apply a fixed threshold to binarize the most probable region. Of note, no over-tuning of this parameter was not applied and a different value could be also used without losing performance. Different threshold strategies with extra terms (such as area, maximum length, adaptive approach) could be an interesting solution to improve the method's performance. Nevertheless, we would like to emphasize that the maximum probability's position was included inside the manual FO surfaces (by both observers), corroborating the method's accuracy.

Figure 7 allows one to conclude that the FA method presented a performance similar to the inter-observer variability for the FO identification, validating the potential of the proposed method. Statistically significant differences were found between the intra-observer

variability and the remaining cases, which can be explained by the small number of cases used and even by different manual delineation strategies applied. While one of the observers tended to segment the inner portion of the central depression of the FO only, the second one included both FO and the initial transition of the FO limbus, obtaining a larger contour. Interestingly, our automatic strategy typically generates a contour at the intermediate position of both manual contours (Figure 9). The CPE results corroborated the high accuracy of the proposed automatic method, particularly, considering the mean size - 17±2.7 mm - of the FO in the test database, but with statistically significant differences against the inter-observer variability, which indicates a misalignment between manual and FA surfaces. These differences can be explained by the sub-optimal segmentation result at the top of the atrial roof, due to its high curvature and its irregular shape (white arrow on Figure 6c and Figure 9e). These last observations are corroborated by Figure 8, where it is depicted that the manual centroid positions are typically located superiorly (at the coronal and sagittal directions) than the centroid of the automatic result.

The authors would like to emphasize that although the proposed methodology, focused on anatomical alignment and contour refinement, proved its high accuracy and robustness for the segmentation of the atrial region (mainly at the thin mid atrial walls) and fossa ovalis, different solutions based on machine learning approaches (principally deep learning techniques) are also potentially interesting. Indeed, such solutions are expected to be developed during the next years, both for the segmentation of the cardiac chambers and even for the fossa ovalis region. Nevertheless, when comparing end-to-end deep learning approaches with the proposed technique, there are several challenges that need to be addressed in the near future: 1) to the author's best knowledge, large training databases or even benchmarks with strong manual references delineated by multiple observers are not available for this problem; 2) due to its low thickness (in some situations could be one pixel or even not visible), correct modelling of the inter-atrial is not straightforward with the pure machine learning approach, requiring further research; and 3) method's sensitivity to image artifacts (e.g. pacemakers) or abnormal anatomies (possibly not represented in the training database) needs to be studied.

As a future work, we intend to apply the proposed framework for real planning of inter-atrial intervention [9, 22]. Not only the physician will use the automatically estimated

surfaces to identify the optimal path, as also the obtained models will be included in the real intervention (combining fluoroscopy and CT data through [9]), improving the interventional data and easing the identification of relevant anatomical regions. The FO will be represented as an accurate 3D surface, representing its entire shape and not only one specific point [37], easing the selection of the optimal route and preventing procedural complications/failures [5, 6]. Furthermore, we also believe that our method could also be applied to improve IAS intervention simulation tools [23], by applying realistic and accurate models of the atrial region and the FO, instead of mean atrial region models or entire IAS wall surfaces. Finally, the proposed fully-automatic atrial region segmentation strategy can be efficiently applied in clinical practice for accurate evaluation of the relevant global indicators (e.g., volume, dimension) of the LA, RA and AO. Moreover, although it was not within the scope of the current study, the current fully-automatic methodology can be extended, keeping its high accuracy and robustness, for other cardiac chambers (e.g. LV) or even different imaging modalities (e.g. 3D magnetic resonance imaging, requiring only a different atlas database), thereby increasing the potential of the proposed framework for the clinical environment. Nevertheless, and as explained in our previous study [18], segmentation of the RV with the current atlas-based approach followed by competitive BEAS is not feasible. Since BEAS relies on explicit functions, intrinsic shape limitations are imposed (e.g. spherical or cylindrical space), being therefore – in its present form - not suitable to describe complex anatomies as the RV.

The current study has some limitations, namely: 1) accurate identification of FO is unfeasible on non-contrasted CT or datasets with larger pixel spacing due to the low contrast and resolution of the thin IAS wall (as a consequence, a non-refined IAS_{wall} map is obtained), respectively; 2) extreme abnormal atrial anatomies can present a sub-optimal result when performing the atlas alignment or when estimating the $FO_{Spatial}$ map due to the limited shape representation on the reference templates; 3) a sub-optimal FO result can be obtained in patients with patent foramen ovale; and 4) a larger and multi-center database with manual references from several experts is required to exhaustive validate the proposed pipeline.

5. Conclusions

The proposed fully automatic framework showed its promising for IAS interventional planning, making the planning more accurate, simpler, without observer variability and

faster. The new atrial region segmentation approach obtained results comparable to the remaining state-of-the-art methods, but providing superior results for the mid atrial walls. No differences were found between the new and our previous segmentation approaches; however, it should be noted that with the new approach, the segmentation is free of user interaction. Regarding the fossa ovalis segmentation, the proposed method obtained results similar to the ones manually delineated by experts, allowing a correct and fast identification of the optimal route for transseptal puncture or optimal device selection for LA interventions.

Acknowledgements

References

[1] R.H. Anderson, R. Razavi, A.M. Taylor, Cardiac anatomy revisited, Journal of Anatomy, 205 (2004) 159-177.

[2] C. Tobon-Gomez, A.J. Geers, J. Peters, J. Weese, K. Pinto, R. Karim, M. Ammar, A. Daoudi, J. Margeta, Z. Sandoval, Benchmark for algorithms segmenting the left atrium from 3D CT and MRI datasets, IEEE transactions on medical imaging, 34 (2015) 1460-1473.

[3] T.H. Hauser, D.C. Peters, J.V. Wylie, W.J. Manning, Evaluating the left atrium by magnetic resonance imaging, Europace, 10 (2008) iii22-iii27.

[4] W.P. Abhayaratna, J.B. Seward, C.P. Appleton, P.S. Douglas, J.K. Oh, A.J. Tajik, T.S. Tsang, Left atrial size: physiologic determinants and clinical applications, Journal of the American College of Cardiology, 47 (2006) 2357-2363.

[5] P. Morais, J.L. Vilaça, J. Ector, J. D'hooge, J.M.R. Tavares, Novel solutions applied in transseptal puncture: a systematic review, Journal of Medical Devices, 11 (2017) 010801.

[6] V.C. Babaliaros, J.T. Green, S. Lerakis, M. Lloyd, P.C. Block, Emerging Applications for Transseptal Left Heart CatheterizationOld Techniques for New Procedures, Journal of the American College of Cardiology, 51 (2008) 2116-2122.

[7] K. Cleary, T.M. Peters, Image-guided interventions: technology review and clinical applications, Annual review of biomedical engineering, 12 (2010) 119-142.

[8] Y. Yao, L. Ding, W. Chen, J. Guo, J. Bao, R. Shi, W. Huang, S. Zhang, T. Wong, The training and learning process of transseptal puncture using a modified technique, Europace, (2013) eut078.

[9] F. Bourier, T. Reents, S. AMMAR-BUSCH, V. Semmler, M. Telishevska, M. Kottmaier, C. Lennerz, C. Grebmer, C. Kolb, I. Deisenhofer, Transseptal Puncture Guided by CT-Derived 3D-Augmented Fluoroscopy, Journal of cardiovascular electrophysiology, (2016).

[10] R. Liao, S. Miao, Y. Zheng, Automatic and efficient contrast-based 2-D/3-D fusion for trans-catheter aortic valve implantation (TAVI), Computerized Medical Imaging and Graphics, 37 (2013) 150-161.

[11] J.J. Thaden, S. Sanon, J.B. Geske, M.F. Eleid, N. Nijhof, J.F. Malouf, C.S. Rihal, C.J. Bruce, Echocardiographic and fluoroscopic fusion imaging for procedural guidance: an overview and early clinical experience, Journal of the American Society of Echocardiography, 29 (2016) 503-512.

[12] X. Huang, J. Moore, G. Guiraudon, D.L. Jones, D. Bainbridge, J. Ren, T.M. Peters, Dynamic 2D ultrasound and 3D CT image registration of the beating heart, Medical Imaging, IEEE Transactions on, 28 (2009) 1179-1189.

[13] S. Queiros, A. Papachristidis, P. Morais, K.C. Theodoropoulos, J.C. Fonseca, M.J. Monaghan, J.L. Vilaca, J. D'hooge, Fully automatic 3D-TEE segmentation for the planning of Transcatheter Aortic Valve Implantation, IEEE Transactions on Biomedical Engineering, 64 (2016) 1711-1720.

[14] O. Ecabert, J. Peters, M.J. Walker, T. Ivanc, C. Lorenz, J. von Berg, J. Lessick, M. Vembar, J. Weese, Segmentation of the heart and great vessels in CT images using a model-based adaptation framework, Medical image analysis, 15 (2011) 863-876.

[15] Y. Zheng, A. Barbu, B. Georgescu, M. Scheuering, D. Comaniciu, Four-chamber heart modeling and automatic segmentation for 3-D cardiac CT volumes using marginal space learning and steerable features, Medical Imaging, IEEE Transactions on, 27 (2008) 1668-1681.

[16] H. Kirişli, M. Schaap, S. Klein, S. Papadopoulou, M. Bonardi, C.-H. Chen, A. Weustink, N. Mollet, E. Vonken, R. van der Geest, Evaluation of a multi-atlas based method for segmentation of cardiac CTA data: a large-scale, multicenter, and multivendor study, Medical Physics, 37 (2010) 6279-6291.

[17] M.A. Zuluaga, M.J. Cardoso, M. Modat, S. Ourselin, Multi-atlas propagation whole heart segmentation from MRI and CTA using a local normalised correlation coefficient criterion, Functional Imaging and Modeling of the Heart, Springer2013, pp. 174-181.

[18] P. Morais, J.L. Vilaça, S. Queirós, F. Bourier, I. Deisenhofer, J.M.R.S. Tavares, J. D'Hooge, A competitive strategy for atrial and aortic tract segmentation based on deformable models, Medical Image Analysis, 42 (2017) 102-116.

[19] R. Shahzad, D. Bos, R.P. Budde, K. Pellikaan, W.J. Niessen, A. van der Lugt, T. van Walsum, Automatic segmentation and quantification of the cardiac structures from non-contrast-enhanced cardiac CT scans, Physics in Medicine and Biology, 62 (2017) 3798.

[20] Y. Wang, L. Di Biase, R.P. Horton, T. Nguyen, P. Morhanty, A. Natale, Left atrial appendage studied by computed tomography to help planning for appendage closure device placement, Journal of cardiovascular electrophysiology, 21 (2010) 973-982.

[21] F.F. Faletra, L. Biasco, G. Pedrazzini, M. Moccetti, E. Pasotti, L.A. Leo, G. Cautilli, T. Moccetti, M.J. Monaghan, Echocardiographic-Fluoroscopic Fusion Imaging in Transseptal Puncture: A New Technology for an Old Procedure, Journal of the American Society of Echocardiography, 30 (2017) 886-895.

[22] S. Verma, S. Adler, A. Berman, A. Duran, D. Loar, Localization of fossa ovalis and Brockenbrough needle prior to left atrial ablation using three-dimensional mapping with EnSite Fusion™, Journal of Interventional Cardiac Electrophysiology, 30 (2011) 37-44.

[23] J. Jayender, R.V. Patel, G.F. Michaud, N. Hata, Optimal transseptal puncture location for robot-assisted left atrial catheter ablation, The International Journal of Medical Robotics and Computer Assisted Surgery, 7 (2011) 193-201.

[24] J.E. Iglesias, M.R. Sabuncu, Multi-atlas segmentation of biomedical images: a survey, Medical image analysis, 24 (2015) 205-219.

[25] N. Otsu, A threshold selection method from gray-level histograms, Automatica, 11 (1975) 23-27.

[26] S. Queirós, D. Barbosa, B. Heyde, P. Morais, J.L. Vilaça, D. Friboulet, O. Bernard, J. D'hooge, Fast Automatic Myocardial Segmentation in 4D cine CMR datasets, Medical image analysis, 18 (2014) 1115-1131.

[27] D. Barbosa, T. Dietenbeck, J. Schaerer, J. D'hooge, D. Friboulet, O. Bernard, B-spline explicit active surfaces: An efficient framework for real-time 3-D region-based segmentation, Image Processing, IEEE Transactions on, 21 (2012) 241-251.

[28] J. Pedrosa, D. Barbosa, B. Heyde, F. Schnell, A. Rösner, P. Claus, J. D'hooge, Left Ventricular Myocardial Segmentation in 3-D Ultrasound Recordings: Effect of Different Endocardial and Epicardial Coupling Strategies, IEEE transactions on ultrasonics, ferroelectrics, and frequency control, 64 (2017) 525-536.

[29] B. Amberg, S. Romdhani, T. Vetter, Optimal step nonrigid icp algorithms for surface registration, Computer Vision and Pattern Recognition, 2007. CVPR'07. IEEE Conference on, IEEE, 2007, pp. 1-8.

[30] A.H. Squillacote, J. Ahrens, The paraview guide, Kitware2007.

[31] S. Klein, M. Staring, K. Murphy, M.A. Viergever, J.P. Pluim, Elastix: a toolbox for intensity-based medical image registration, IEEE transactions on medical imaging, 29 (2010) 196-205.

[32] I. Wolf, M. Vetter, I. Wegner, T. Böttger, M. Nolden, M. Schöbinger, M. Hastenteufel, T. Kunert, H.-P. Meinzer, The medical imaging interaction toolkit, Medical image analysis, 9 (2005) 594-604.

[33] P. Wagdi, H. Alkadhi, Can computer tomography help predict feasibility of transseptal puncture after percutaneous closure of an interatrial septal communication?, Journal of Interventional Cardiac Electrophysiology, 34 (2012) 167-172.

[34] S. Knecht, H. Skali, M.D. O'neill, M. Wright, S. Matsuo, G.M. Chaudhry, C.I. Haffajee, I. Nault, G.H. Gijsbers, F. Sacher, Computed tomography–fluoroscopy overlay evaluation during catheter ablation of left atrial arrhythmia, Europace, 10 (2008) 931-938.

[35] S. Queirós, C. Dubois, P. Morais, T. Adriaenssens, J.C. Fonseca, J.L. Vilaça, J. D'hooge, Automatic 3D aortic annulus sizing by computed tomography in the planning of transcatheter aortic valve implantation, Journal of Cardiovascular Computed Tomography, (2016).

[36] S. Knecht, I. Nault, M. Wright, S. Matsuo, N. Lellouche, P.E. Somasundaram, M.D. O'neill, K.-T. Lim, F. Sacher, A. Deplagne, Imaging in catheter ablation for atrial fibrillation: enhancing the clinician's view, Europace, 10 (2008) iii2-iii7.

[37] L.N. Graham, I.C. Melton, S. MacDonald, I.G. Crozier, Value of CT localization of the fossa ovalis prior to transseptal left heart catheterization for left atrial ablation, Europace, 9 (2007) 417-423.

[38] D.R. Tomlinson, N. Sabharwal, Y. Bashir, T.R. Betts, Interatrial septum thickness and difficulty with transseptal puncture during redo catheter ablation of atrial fibrillation, Pacing and Clinical Electrophysiology, 31 (2008) 1606-1611.

[39] F.F. Faletra, G. Perk, N.G. Pandian, H.-J. Nesser, I. Kronzon, Closure of Patent Foramen Ovalis and Atrial Septal Defect, Real-Time 3D Interventional Echocardiography, Springer2014, pp. 21-41.

Multimedia Material I – Coupling approach

    B – Spline Explicit Active Surface (BEAS): The BEAS framework represents the different contours as explicit functions, which means that one of the coordinates of the points of the interface, $\boldsymbol{x} = \{x_1, x_2, ..., x_N\}$ in a N-dimensional space, is expressed as a function of the remaining coordinates (*i.e.* $\boldsymbol{x}^* = \{x_2, ..., x_N\}$) reducing therefore, the dimensionality of the segmentation problem. Consequently, each explicit function ψ_i ($i \in \{LA, RA, AO\}$) is defined as (Almeida et al., 2016):

$$\psi_i(\boldsymbol{x}^*) = \sum_{k \in \mathbb{Z}^{N-1}} c_i[\boldsymbol{k}] \beta_i^d \left(\frac{\boldsymbol{x}^* - \boldsymbol{k} h_{r_i}}{h_{s_i}} \right), \tag{1}$$

where $\beta_i^d(\cdot)$ is the uniform symmetric $(N-1)$-dimensional B-spline of degree d of each contour i. The knots of the B-splines are located on a regular grid defined on a specific space; h_s and h_r are smoothness parameters that control the scaling and spacing of the B-spline kernel, respectively; $c_i[\boldsymbol{k}]$ are the B-spline coefficients of contour i.

    As previously described in our initial work (Morais et al., 2017), the evolution of each contour i is independently controlled, and finally combined through:

$$E = \sum_i E_i,$$

$$E_i = \int_\Omega \delta_{\phi_i}(\boldsymbol{x}) \int_\Omega B(\boldsymbol{x}, \boldsymbol{y}).F_i(\boldsymbol{y}) d\boldsymbol{y} d\boldsymbol{x}, \tag{2}$$

where $\phi_i(\boldsymbol{x}) = \Gamma_i(\boldsymbol{x}^*) - x_1$, $i \in \{LA, RA, AO\}$ with n representing the total number of contours, $\boldsymbol{x}, \boldsymbol{y}$ are independent spatial locations in the image domain Ω, $\phi_i(\boldsymbol{x})$ is a level-set like function representing the region inside the interface Γ_i, δ_{ϕ_i} is the Dirac function and F_i an image criteria (e.g. localized Chan-Vese energy (Lankton and Tannenbaum, 2008)); $B(\boldsymbol{x}, \boldsymbol{y})$ corresponds to a mask function in which the regional parameters that locally drive the contour evolutions are computed. In order to identify the optimal contour positions, energy E is minimized through the computation of the energy derivatives with respect to each $c_i[\boldsymbol{k}]$, as described in (Barbosa et al., 2012):

$$\frac{\partial E_i}{\partial c_i[\boldsymbol{k}]} = \int_{\Gamma_i} \bar{g}_i(\boldsymbol{x}^*) \beta_i^d \left(\frac{\boldsymbol{x}^* - \boldsymbol{k} h_{r_i}}{h_{s_i}} \right) d\boldsymbol{x}^*, \tag{3}$$

with $\bar{g}_i(\boldsymbol{x}^*)$ representing the feature map (e.g. first derivative of the local Chan-Vese energy, (Lankton and Tannenbaum, 2008)) of each contour i.

    Coupling strategy: Starting from the obtained LA contour (see "Competitive Segmentation" section in the article), an extra BEAS surface representing the wall thickness is initialized (henceforward referred as IAS wall contour), meaning that $i \in \{LA, RA, AO, IAS\}$.

    The IAS contour is defined based on the LA contour (*i.e.* same centroid) plus a constant thickness (here of 5 mm, Figure 1a). Instead of the free evolution of the IAS contour, we decided to combine it with the LA surface. Therefore, the IAS contour is modeled as a combination of two explicit functions representing the LA position (ψ^{Pos}) and IAS wall thickness (ψ^{Thick}), respectively (Figure 1). In detail, the IAS contour (S_{IAS}) is now described as (Pedrosa et al. 2017):

$$S_{IAS}(\boldsymbol{x}^*) = \Gamma_{IAS}(\boldsymbol{x}^*) = \psi^{Pos}(\boldsymbol{x}^*) + \psi^{Thick}(\boldsymbol{x}^*), \tag{4}$$

$$\psi_{i,t=0}^{Pos} = \psi_{i,t=1}^{Pos} = \psi_{i,t=2}^{Pos} \qquad \psi_{i,t=0}^{Thick} \neq \psi_{i,t=1}^{Thick} \neq \psi_{i,t=2}^{Thick} \qquad i \in [1 - m]$$
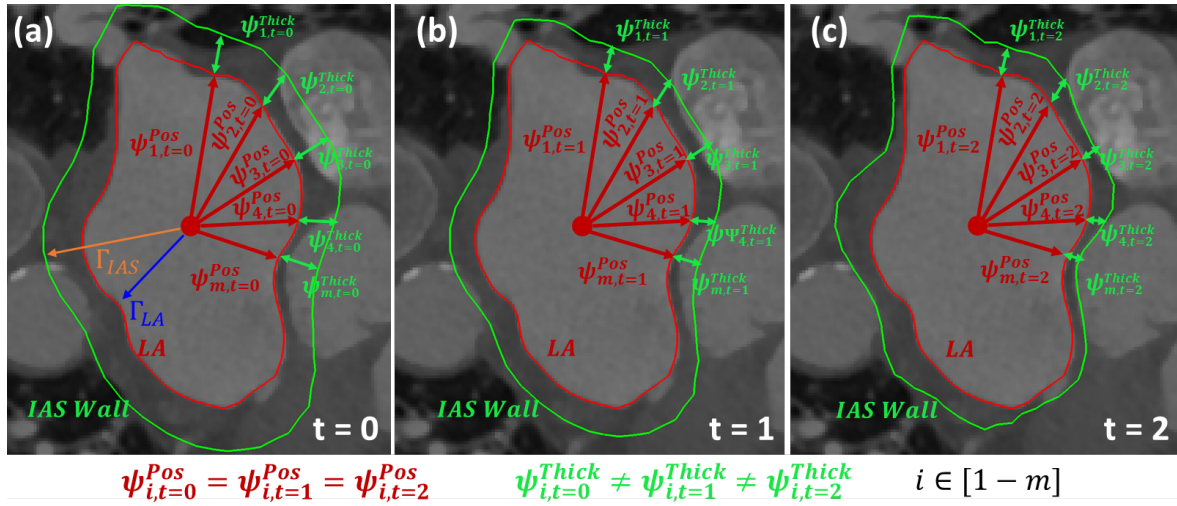
Figure 1 – Illustration of the coupling strategy: The IAS wall contour is described based on the LA position (ψ^{Pos}) plus the wall thickness (ψ^{Thick}); Algorithm's result at temporal moment (a) 0; (b) 1 and (c) 2. (Please note that the LA contour (red) is not modified.)

and the energy derivatives as:

$$\frac{\partial E_{IAS}}{\partial c_{IAS}[\boldsymbol{k}]} = \int_{\Gamma_{IAS}} \bar{g}_{IAS}^{Pos}(\boldsymbol{x}^*)\beta_{IAS}^d\left(\frac{\boldsymbol{x}^* - \boldsymbol{k}h_{r_{IAS}}}{h_{s_{IAS}}}\right)d\boldsymbol{x}^* + \int_{\Gamma_{IAS}} \bar{g}_{IAS}^{Thick}(\boldsymbol{x}^*)\beta_{IAS}^d\left(\frac{\boldsymbol{x}^* - \boldsymbol{k}h_{r_{IAS}}}{h_{s_{IAS}}}\right)d\boldsymbol{x}^*, \quad (5)$$

where $\bar{g}_{IAS}^{Pos}$ and $\bar{g}_{IAS}^{Th}$ represent the feature map of the wall surface position and wall thickness, respectively. Moreover, it should be noted that LA contour is equal to ψ^{Pos}.

Since the LA contour is only used as an anchor, keeping its original position throughout this algorithm step, ψ^{Pos} is kept unaltered (Figure 1). Therefore, equation (6) can be described as:

$$\frac{\partial E_{IAS}}{\partial c_{IAS}[\boldsymbol{k}]} = \int_{\Gamma_{IAS}} \bar{g}_{IAS}^{Thick}(\boldsymbol{x}^*)\beta_{IAS}^d\left(\frac{\boldsymbol{x}^* - \boldsymbol{k}h_{r_{IAS}}}{h_{s_{IAS}}}\right)d\boldsymbol{x}^*. \quad (6)$$

It should be noted that the IAS wall contour is only estimated based on wall thickness parameter and not directly on the final wall position (Figure 1). Such strategy prevents irregular regions caused by low contrast and even missing walls.

Finally, since the IAS wall segmentation is only applied after the atrial region segmentation, being the atrial region contour not altered at this step, the evolution energy is only represented as:

$$E = E_{IAS}. \quad (7)$$

References:

Almeida, N., Friboulet, D., Sarvari, S.I., Bernard, O., Barbosa, D., Samset, E., D'hooge, J., 2016. Left-Atrial Segmentation From 3-D Ultrasound Using B-Spline Explicit Active Surfaces With Scale Uncoupling. IEEE transactions on ultrasonics, ferroelectrics, and frequency control 63, 212-221.

Barbosa, D., Dietenbeck, T., Schaerer, J., D'hooge, J., Friboulet, D., Bernard, O., 2012. B-spline explicit active surfaces: An efficient framework for real-time 3-D region-based segmentation. Image Processing, IEEE Transactions on 21, 241-251.

Lankton, S., Tannenbaum, A., 2008. Localizing region-based active contours. Image Processing, IEEE Transactions on 17, 2029-2039.

Morais P., Vilaça, J. L., Queirós, S., Bourier, F., Deisenhofer, I., Tavares, JMRS, D'hooge, J., "A competitive strategy for atrial and aortic tract segmentation based on deformable models," *Medical Image Analysis*, 2017.

Pedrosa, J., Barbosa, D., Heyde, B., Schnell, F., Rosner, A., Claus, P., 2016. Left Ventricular Myocardial Segmentation in 3D Ultrasound Recordings: Effect of Different Endoand Epicardial Coupling Strategies. IEEE Transactions on Ultrasonics, Ferroelectrics, and Frequency Control.

Multimedia Material II – Representative cases of the used clinical database
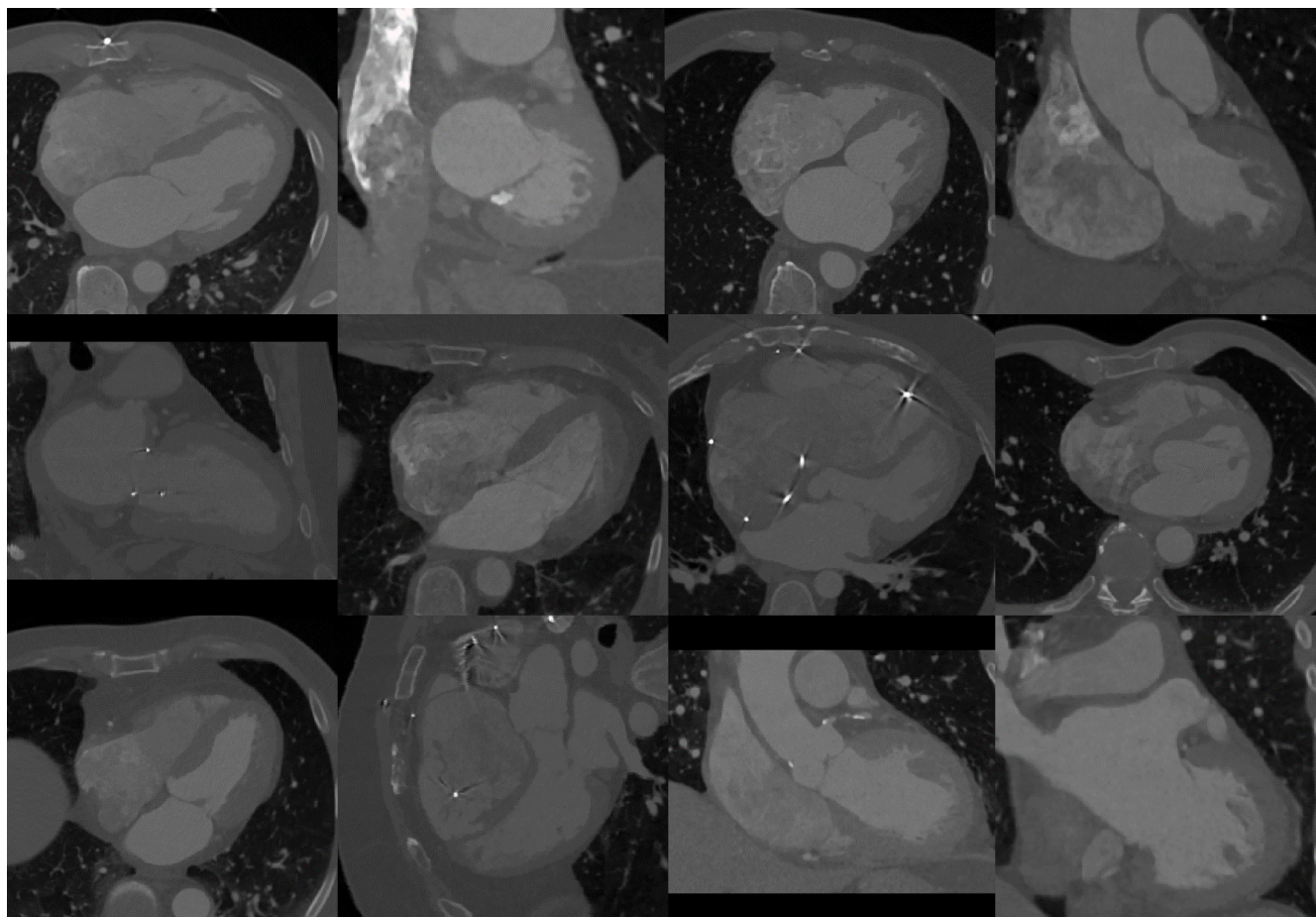
Figure 1 – Representative cases of the test clinical database.

Multimedia Material III

<u>Data Description:</u> The 41 clinical datasets described in the article were used.

<u>Experiments and Results:</u> A parameter tuning analysis of the proposed fully automatic method to identify the fossa ovalis (FO) is presented. First, the influence of the multiple maps (*i.e.* thickness and spatial information maps generated throughout sections II-D-1 and II-D-2, respectively) was assessed. Next, the influence of the transformation model (*i.e.*, rigid, affine or similarity) applied on the iterative closest point (ICP) algorithm (section II-D-2) and also the threshold used to binarize the FO region was evaluated. All the parameter pairs were compared through a paired t-test (p<0.05). Finally, the influence of the number of templates used to estimate the spatial map ($FO_{Spatial}$) was also investigated.

Figure 1a shows the influence of the different steps of the new identification algorithm, proving that a superior performance is obtained when both maps (*i.e.* thickness and spatial location) are combined.
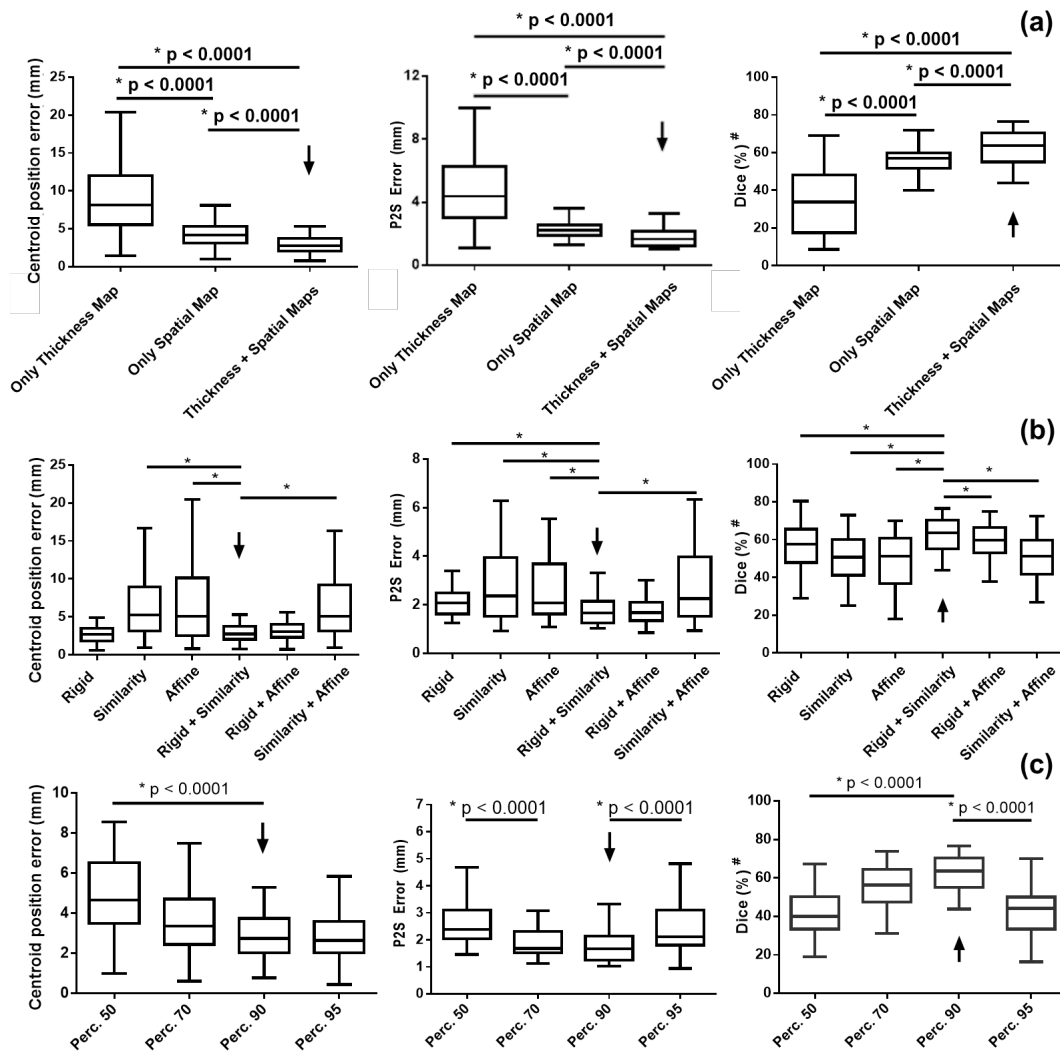

*Figure 1 – Sensitivity analysis of the different parameters and algorithm's step described in the fossa ovalis (FA) automatic identification strategy: a) Evaluate the influence of the thickness and spatial location maps; b) assess the method's accuracy with different transformation applied in the surface alignment step; and c) shows the influence of the selected threshold to binarize the FO position. (The centroid position error (first column), point-to-surface (P2S, second column) error and Dice (third column) were used as evaluation metrics. The arrow identifies the selected parameter; * p<0.05 with a paired t-test between all the parameters' pairs; # - Cases without surface's overlap were excluded.)*

In one hand, the results proved that the thickness map is sensitive to local minima found throughout the entire left atrial surface. On the other hand, the spatial map is able to roughly detect the FO region, failing to refine the result to the target anatomy, which is achieved by combining the spatial and thickness maps. Figure 1b evaluates the different transformation models applied in the surface alignment through ICP. Globally, the results proved that a double alignment strategy, where both surfaces are initially rigidly aligned and then its sizing differences compensated through a similarity or affine model, achieved the best performance with statistically significant differences when compared with the other possibilities. Finally, the influence of the threshold (described in section II-D-3) is presented in Figure 1c. The results proved that a different value (varying between the percentile 70th and 90th) could be applied without statistically significant differences.

Figure 2 shows the point-to-surface (P2S) error evolution with the variation of the total number of templates (required on section II-D-2 for the $FO_{Spatial}$ map estimation). It should be noted that for all the possibilities, the reference database was always constructed without the target case. An increase of the P2S errors was observed when a small number of templates are used (~less than 10 cases), which is explained by the voting strategy applied on the $FO_{Spatial}$ map estimation step and the limited shape variability. Indeed, due to the limited number of samples, a sparse $FO_{Spatial}$ map was obtained (caused by sub-optimal alignment results), preventing a correct estimation of the FO region. In opposition, a similar performance with high accuracy was obtained for cases with a high number of templates (20-40 samples, with 40 representing the entire template database). This result reinforces the advantages of the proposed method, showing that $FO_{Spatial}$ map is only required to estimate the most probably spatial location of the FO region being posteriorly refined using patient-specific information extracted from the IAS_{Map}. When using a high number of templates (more than 20, *i.e.* half of the entire reference database), the influence of sub-optimal results is minimized and the most common region is therefore, enhanced (*i.e.* region where a high number of templates will vote as optimal position). Nevertheless, a notable improvement of the method's accuracy is not predictable with the increase of the total database (*i.e.* more than 40). In fact, it is only expected a slight enhancement of the optimal FO region.
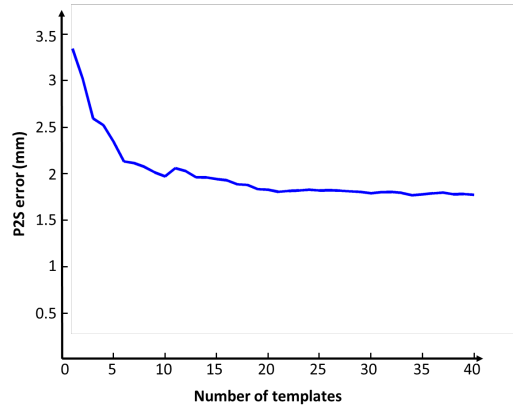

Figure 2 – *Influence of the total number of templates used throughout the $FO_{Spatial}$ map estimation in the final accuracy of the new fossa ovalis identification approach.*

Multimedia Material IV

Data Description: The accuracy of the proposed fully automatic segmentation method was evaluated using a public available benchmark database (STACOM 2013). The public database has thirty datasets, 10 datasets for training and 20 datasets for testing. Only left atrial (LA) contours are allowed to be evaluated with the current benchmark. The reader is kindly directed to the original work (Tobon-Gomez *et al.*, 2015) for further details on imaging acquisition and ground truth generation.

Experiments and Results: The proposed fully automatic method (FA) was applied successfully to segment the LA in all the datasets. Its results were compared with the ones of other state-of-the-art techniques in terms of point-to-distance (P2S) and Dice coefficient. Although a total of 9 works was initially evaluated in this challenge, only the 5 best results are presented and compared with the FA method. Moreover, the SA version of the proposed competitive strategy (Morais *et al.*, 2017) is also presented and directly compared with the FA method through an unpaired t-test ($p<0.05$).

The proposed FA method obtained a P2S error of 0.85±1.02 mm, proving its robustness and accuracy with a performance similar to the remaining state-of-the-art methods; namely, machine learning, atlas-based and deformable models based methods, Figure 1. Moreover, no statistically significant differences were found between the FA and SA methods, corroborating the method's accuracy. Finally, since the proposed method is totally automatic (no user interaction) and fast (less than 2 minutes in a common personal laptop computer), it proved its added-value for normal clinical practice.

LTSI_VRG – (Sandoval *et al.*, 2013); LUB_SRG – (Stender *et al.*, 2013);
SIE_PMB and SIE_MRG – (Zheng *et al.*, 2008); UCL_1C – (Zuluaga *et al.*, 2013)

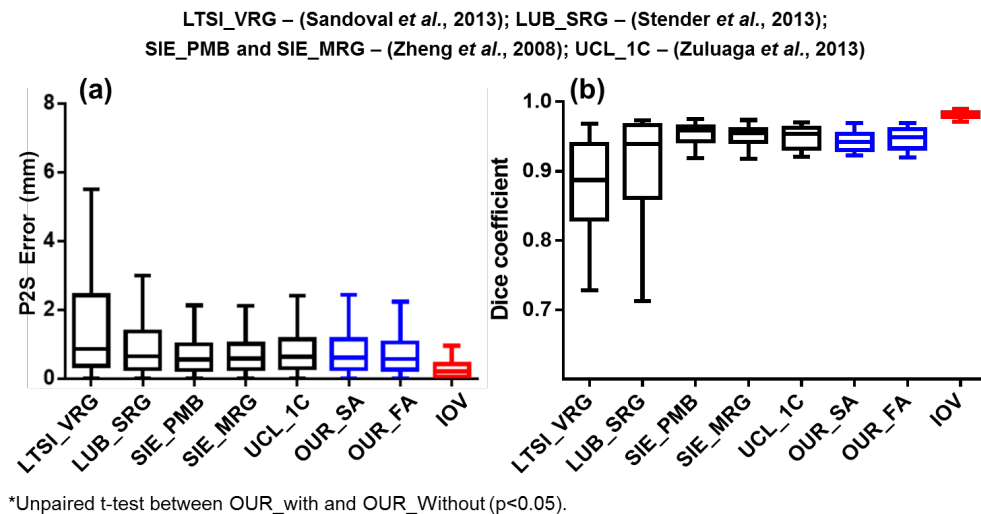*Unpaired t-test between OUR_with and OUR_Without ($p<0.05$).

Figure 1 - Assessment of the proposed fully automatic method for left atrium segmentation in CT data and comparison against the best results available in the public available benchmark. Moreover, the performance of our previous developed semi-automatic method is also presented. (Each team's name was defined based on [34]; IOV represents the inter-observer variability.)

References:

Morais, P., Vilaça, J. L., Queirós, S., Bourier, F., Deisenhofer, I., Tavares, J. M. R. S., D'hooge, J., "A competitive strategy for atrial and aortic tract segmentation based on deformable models," Medical image analysis (submitted), 2017.

Sandoval, Z., Betancur, J., Dillenseger, J.-L., 2013. Multi-atlas-based segmentation of the left atrium and pulmonary veins, International Workshop on Statistical Atlases and Computational Models of the Heart. Springer, pp. 24-30.

Stender, B., Blanck, O., Wang, B., Schlaefer, A., 2013. Model-Based Segmentation of the Left Atrium in CT and MRI Scans, International Workshop on Statistical Atlases and Computational Models of the Heart. Springer, pp. 31-41.

Tobon-Gomez, C., Geers, A.J., Peters, J., Weese, J., Pinto, K., Karim, R., Ammar, M., Daoudi, A., Margeta, J., Sandoval, Z., 2015. Benchmark for algorithms segmenting the left atrium from 3D CT and MRI datasets. IEEE transactions on medical imaging 34, 1460-1473.

Zheng, Y., Barbu, A., Georgescu, B., Scheuering, M., Comaniciu, D., 2008. Four-chamber heart modeling and automatic segmentation for 3-D cardiac CT volumes using marginal space learning and steerable features. IEEE Transactions on Medical Imaging, 27, 1668-1681.

Zuluaga, M.A., Cardoso, M.J., Modat, M., Ourselin, S., 2013. Multi-atlas propagation whole heart segmentation from MRI and CTA using a local normalised correlation coefficient criterion, Functional Imaging and Modeling of the Heart. Springer, pp. 174-181.